

# Robustness Optimization for Compact Free-electron Laser Driven by Laser Wakefield Accelerators

Hai Jiang,<sup>1,2</sup> Ke Feng,<sup>2,\*</sup> Runshu Hu,<sup>2,3</sup> Qiwen Zhan,<sup>1,†</sup> Wentao Wang,<sup>2,‡</sup> and Ruxin Li<sup>2,4,3</sup>

<sup>1</sup>*School of Optical-Electrical and Computer Engineering,*

*University of Shanghai for Science and Technology, Shanghai 200093, People's Republic of China*

<sup>2</sup>*State Key Laboratory of High Field Laser Physics and CAS Center for Excellence in Ultra-intense Laser Science,*  
*Shanghai Institute of Optics and Fine Mechanics (SIOM),*

*Chinese Academy of Sciences (CAS), Shanghai 201800, People's Republic of China*

<sup>3</sup>*Center of Materials Science and Optoelectronics Engineering,*

*University of Chinese Academy of Sciences, Beijing 101408, People's Republic of China*

<sup>4</sup>*School of Physical Science and Technology, ShanghaiTech University, Shanghai 201210, People's Republic of China*

(Dated: March 18, 2025)

Despite the successful demonstration of compact free electron lasers (FELs) driven by laser wakefield accelerators (LWFAs), the shot-to-shot fluctuations inherent to LWFAs remain a major obstacle to realizing LWFA-driven FELs with high gain and robust operation. Here, we present a conceptual design for LWFA-driven FELs with enhanced robustness and reliability. By employing Bayesian optimization techniques, the beamline was optimized to achieve sufficient tolerance against these fluctuations under actual experimental conditions. Start-to-end simulations revealed that this systematic optimization significantly reduces the system's sensitivity to parametric variations. With the optimized configurations, the radiation energy can be maintained above 1  $\mu\text{J}$  at a wavelength of approximately 25 nm, even when accounting for twice the root-mean-square (RMS) ranges of these inherent jitters. This proposed scheme represents a substantial advancement in the development of compact LWFA-driven FEL systems, enabling robust operation and paving the way for the realization of reliable and widely accessible sources.

Free electron lasers (FELs) are capable of generating high-brilliance and coherent radiation across a broad range of wavelengths, extending even into the hard X-ray regime [1–5]. Their unique capabilities hold the potential to revolutionize various scientific disciplines by enabling unparalleled atomic resolutions on femto-to-attosecond timescales [6, 7]. These FEL facilities typically rely on the radio-frequency (RF) accelerators with large scales and incurs exorbitant costs. With unprecedented accelerating gradients reaching several hundreds of gigavolt per meter [8, 9], several orders of magnitude higher than those of RF accelerators, laser wakefield accelerators (LWFAs) provide a promising alternative for driving compact FELs. The realization of such compact LWFA-driven FELs has been identified as one of the major challenges in this decade, as addressed in the European Plasma Research Accelerator with eXcellence In Applications (EuPRAXIA) [10]. Motivated by the vast potential of these more accessible and cost-effective systems, numerous innovative schemes and state-of-the-art technologies have been proposed, resulting in significant improvements in beam qualities of the accelerated  $e$  beams from LWFAs [11–20]. Recently, compact FELs driven by LWFAs have been experimentally demonstrated, with the self-amplified spontaneous emission (SASE) configuration at 27 nm and seeded configuration at 269 nm [21, 22]. However, the reliability and reproducibility issues of LWFAs present major obstacle for realizing compact and robust FELs for application [23, 24].

In LWFAs, the interaction between high-intensity laser pulses and plasma constitutes an exceptionally complex

and nonlinear physical process. Minor fluctuations of the experimental conditions, particularly in the drive laser and plasma properties, can cause substantial shot-to-shot fluctuations in  $e$ -beam qualities [11]. Furthermore, these fluctuations in beam qualities, in terms of energy, energy spread and emittance, can lead to varying degrees of beam property degradation during transport through the beamline. These shot-to-shot fluctuations hinder the gain and pose significant robustness challenges for LWFA-driven FELs [23]. To address these challenges, it is imperative to systematically quantify the beam quality fluctuations induced by the inherent jitter of both laser and plasma parameters. Additionally, substantial optimization of the beamline is essential to enhance its tolerance to these shot-to-shot fluctuations, thereby ensuring robustness of LWFA-driven FELs under actual experimental conditions. Bayesian optimization (BO) has emerged as a particularly suitable approach for optimizing such complex nonlinear system with high evaluation costs or prolonged evaluation times, and has been demonstrated as an effective optimization tool in the field of laser-plasma physics and accelerators [25–30].

In this Letter, we present a conceptual design for high-gain LWFA-driven FELs with enhanced robustness and reliability, which is crucial for practical applications. Through detailed numerical simulations, the shot-to-shot fluctuations in beam quality have been quantitatively analyzed, which stem from both laser and plasma parameters, including laser energy variation, focal position displacement induced by wavefront distortion, and shock front position instability in the plasma. To address these

fluctuations, BO techniques were employed for beamline optimization, utilizing the power gain length and FEL energy as the objective function. Start-to-end simulations show that the optimized system can maintain FEL radiation in the saturated or near-saturated regime with corresponding energy exceeding 1  $\mu\text{J}$  in the extreme ultraviolet (EUV) region, even operating within twice the root-mean-square (RMS) range of each parameter jitter. In addition, we conducted a quantitative analysis of the system's tolerance to  $e$  beam pointing jitter, revealing that the proposed scheme can tolerate pointing jitters up to 1 mrad while maintaining FEL radiation energy above 1  $\mu\text{J}$ . This proposed scheme represents a significant advancement in the development of compact LWFA-driven FEL systems with robust operation, offering a promising pathway toward the realization of reliable and widely accessible system.

To investigate the shot-to-shot fluctuations in beam quality generated by LWFAs, quasi-three-dimensional (3D) particle-in-cell (PIC) simulations were conducted using the FBPIC code with a co-moving simulation box [31, 32]. The simulation utilized a Gaussian laser pulse with a central wavelength of  $\lambda = 800$  nm, a waist radius of  $\omega_0 = 35$   $\mu\text{m}$ , a pulse duration of 25 fs (full width at half maximum, FWHM), and a normalized vector potential of  $a_0 = 1.3$ . The plasma density profile was designed based on the previously observed fringe pattern, and the synergistic mechanism of the injection was implemented, as detailed in Ref. [33]. Figure 1(a) illustrates the density profile used in the simulation, with the shock front length configured to 75  $\mu\text{m}$ .

The shot-to-shot fluctuations of the accelerated  $e$  beams primarily originate from inherent jitters in both the laser and plasma. These intrinsic jitters can be quantitatively described by three specific parameters: laser energy variation, focal position displacement caused by wavefront distortion, and shock front position jitter in the plasma. Through systematic experimental measurements, the corresponding RMS values were determined to be  $\Delta E/E = \pm 0.54\%$  for relative laser energy variation [34] and  $\sigma_{zshock} = 4.9$   $\mu\text{m}$  for shock front position jitter, respectively. While the focal position displacement induced by wavefront distortion was not directly measured in our experiments, we adopted a reported value of  $\sigma_{zfoc} = 0.2$  mm according to Ref. [17]. The details of the measured shock front jitter were presented in Appendix A. A comprehensive quantitative characterization of the  $e$ -beam parameters under the influence of these inherent laser and plasma jitters is presented in Figs. 1(b)-1(g), including beam energy, charge, slice energy spread, global energy spread, as well as horizontal and vertical normalized projected emittance. It is noted that the laser energy variation is represented by the variation of laser normalized vector potential  $a_0$  in the following discussions. These jitters span  $\pm 2$  times the measured RMS values in the presented simulations. Each  $e$ -beam pa-

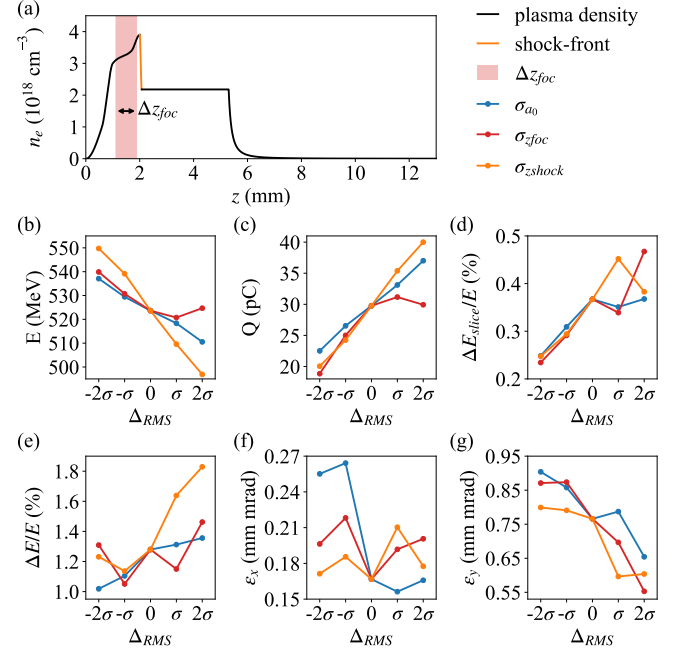


FIG. 1. PIC simulation results of LWFA with inherent parameter jitters obtained from experiments. (a) Schematic of plasma density profile and fluctuation sources, with the pink shaded area region and the orange solid line represent the range of focal position jitter and the initial shock-front position. (b)-(g) Electron beam properties with inherent parameter jitters: the blue, red and orange curves represent the laser energy variations, laser focal position displacement and shock front position instability, respectively. Horizontal axes denotes  $\pm 2$  folds RMS range of these three parameter jitters, and the vertical axes represent beam energy (b), charge (c), slice energy spread (d), global energy spread (e), horizontal (f) and vertical (g) normalized projected emittance.

rameter depicted in Figs. 1(b)- 1(g) containing 13 independent simulation runs, with  $\Delta_{RMS} = 0$  serving as the initial and jitter-free condition.

In the presented simulations, a synergistic mechanism was employed, wherein both the shock front and the self-evolution of the laser contributed to the injection process. By precisely controlling electron injection and chirp compensation through tailored plasma density profiles, high-quality electron beams can be obtained [33]. However, inherent parameter jitter introduces significant instability in electron injection, leading to substantial charge fluctuations. As shown in Fig. 1(c), when accounting for jitter in all three parameters ( $\sigma_{a_0}$ ,  $\sigma_{zfoc}$ , and  $\sigma_{zshock}$ ), the relative charge fluctuation reaches  $\pm 22.0\%$  rms. Such pronounced charge variations induce distinct beamloading effects across different jitter conditions, resulting in variations in acceleration efficiency and inhomogeneities in the accelerating fields. Consequently, the beam quality degrades markedly, with relative energy fluctuation of  $\pm 2.7\%$  rms, slice energy spread fluctuation of  $\pm 21.2\%$  rms, global energy spread fluctuation of  $\pm 17.3\%$  rms,

TABLE I. Parameter space used in  $E_{min}$  optimization.

Parameter	Min. value	Max. value	Best value <sup>a</sup>
$l_0$	0.03	0.2	0.08
$l_1$	0.05	0.2	0.14
$l_2$	0.05	0.2	0.11
$l_3$	0.5	2.0	1.12
$l_4$	1.5	3.0	2.61
$l_5$	0.1	1.0	0.19
$l_6$	0.1	1.0	0.28
$q_1$	-143	-123	-142
$q_2$	123	143	136
$q_3$	-80	-60	-75
$q_4$	-10	10	-2.73
$q_5$	0.0	20	12.94
$q_6$	-20	0.0	-11.55

<sup>a</sup> Note  $l_0 - l_6$  in units of meters (m),  $q_1 - q_6$  in units of per square meter ( $\text{m}^{-2}$ ).

horizontal normalized projected emittance fluctuations of  $\pm 16.2\%$  rms and vertical normalized projected emittance fluctuations of  $\pm 15.1\%$  rms.

These instabilities fundamentally limit the radiation gain and stability of FELs, where achieving high-gain operation typically necessitates three requirements: elevated charge, reduced slice energy spread, and minimized transverse emittance [23]. Our analysis reveals an intrinsic incompatibility among these three metrics, as evidenced by their anti-correlated trends in Figs. 1(c), 1(d) and 1(g). The phase space manipulation of electron beams via beamline optics enables precise control and optimization of beam quality parameters. By leveraging this fundamental principle, strategic design and optimization of the beamline architecture can effectively mitigate beam quality discrepancies, thereby establishing a balanced parameter space essential for generating stable high-gain FEL radiation. This approach addresses a critical factor in maintaining the consistency of FEL performance by compensating for inherent variations in electron beam characteristics through phase space manipulation.

To achieve high-gain LWFA-driven FELs with reliable and robust operations, it is essential to design a beamline with sufficient tolerance to accommodate the shot-to-shot fluctuations of the  $e$  beam induced by experimental jitters, as discussed in Fig. 1. The beamline consists of the following components: three permanent magnetic quadrupoles with a length of 5 cm each, three electromagnetic quadrupoles with a length of 10 cm each, and a 180-period planar undulator with a period length of 25 mm and an undulator parameter of  $K_0 = 1.41$ . These parameters were chosen according to our experimental conditions as reported in Ref. [21, 33]. A BO approach was employed for the beamline optimization. The optimization parameters included the strength parameters of the quadrupoles and the distances between each element, ar-

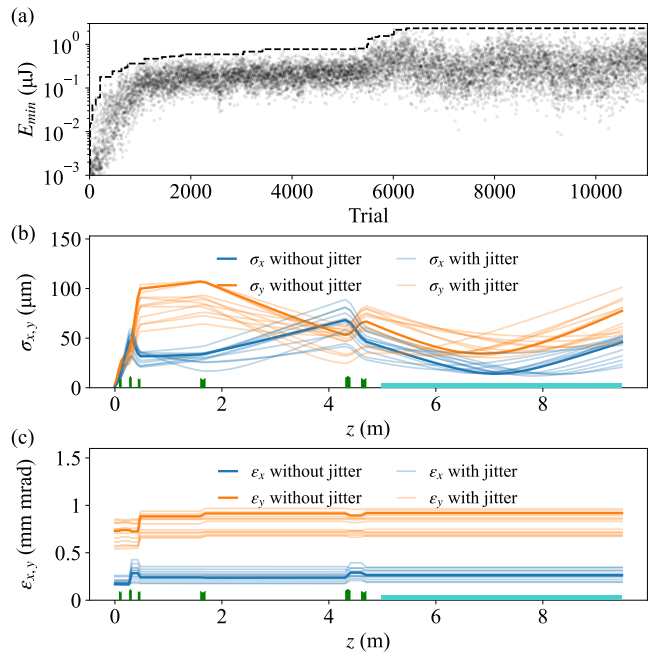


FIG. 2. The optimization results of the  $E_{min}$  for the 13-electron ensemble. (a) The simulated objective function  $E_{min}$  (dots) with the cumulative best results (black dashed line). (b)-(c) The evolution of the beam size (b) and the normalized projected emittance (c) along the beamline in horizontal (blue) and vertical (orange) directions. The tracking beamline was configured using the best parameters obtained from the optimization.

ranged in sequence from upstream to downstream as follows:  $l_0, q_1, l_1, q_2, l_2, q_3, l_3, q_4, l_4, q_5, l_5, q_6, l_6$ . Here,  $l_0$  represents the distance between the gas target and the first quadrupole,  $l_1 - l_5$  denote the distances between adjacent quadrupoles, and  $l_6$  corresponds to the distance between the last quadrupole and the undulator entrance. The variables  $q_1 - q_6$  represent the strength parameters of the quadrupoles.

We employ the Covariance Matrix Adaptation Evolution Strategy (CMA-ES) [35] implemented within the Optuna framework [36] as the primary optimization methodology. Within the context of BO, the formulation of the objective function is of curial importance, as it serves as the mathematical embodiment of our target optimization metric. Here, two distinct objective functions were implemented: the mean reciprocal value of the 3D power gain length  $\langle L_G^{-1} \rangle$  and the minimization of the simulated radiation energy  $E_{min}$  obtained from the 13-electron-beam ensemble shown in Fig. 1. Both objective functions were strategically optimized within a systematic framework to achieve maximization of the desired performance metrics. Before the optimization of FEL radiation energy, we used the  $\langle L_G^{-1} \rangle$  optimization to narrow down the parameters of the beamline components. This constrained parameter space serves prevent-

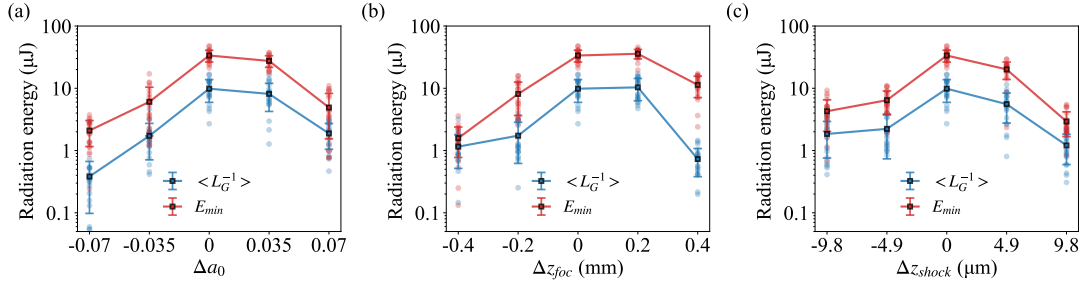


FIG. 3. Radiation energy as a function of (a) normalized vector potential  $\Delta a_0$ , (b) laser focal position  $\Delta z_{foc}$  and (c) the shock-front position  $\Delta z_{shock}$ . Mean values (black squares) and statistical uncertainties (standard deviation) calculated from 20 independent simulations with varying random seeds, where the blue curve represents optimization using  $\langle L_G^{-1} \rangle$  as objective function and the red curve represents optimization using  $E_{min}$  as the objective function.

ing the particle loss event during FEL simulations and enhancing the computational reliability of the optimization process. The details of the  $\langle L_G^{-1} \rangle$  optimization were presented in Appendix B.

In the optimization framework targeting  $E_{min}$ , we conducted parallel particle tracking simulations utilizing the 13-electron-beam ensemble illustrated in Fig. 1. The results of the beam tracking obtained from ELEGANT code [37] served as the input for subsequent FEL simulation performed with 3D and time-dependent code GENESIS [38]. The parameter space for this optimization, detailed in Table I, was systematically refined based on the results from  $\langle L_G^{-1} \rangle$  optimization.

Figure 2(a) illustrates the evolution of the objective function  $E_{min}$  as a function of iterations during the BO process. It should be noted that the radiation energy was obtained by a single run with specific seed for speed-up propose during the optimization process. The optimal solution achieves at iteration 11,020, with the corresponding optimal parameters detailed in Table I. Under these optimized conditions, the radiation energy consistently exceeds 1  $\mu\text{J}$  for all electron beams in the ensemble, indicating robust operation of the LWFA-driven FELs in the saturation or near saturation regime and effectively accommodating shot-to-shot fluctuations. The correspond-

ing evolution of the beam sizes and transverse emittance along the beamline is presented in Figs. 2(b) and 2(c), respectively. Figures 3(a)- 3(c) provide the comparison of the two optimization frameworks targeting  $\langle L_G^{-1} \rangle$  and  $E_{min}$  under their respective optimized conditions. It is noted that the FEL energy was simulated with distinct random seeds for 20 runs in each situation in Fig. 3. While both frameworks exhibit similar trends in radiation energy, the  $E_{min}$  optimized framework demonstrates superior performance with higher radiation energy. This enhancement can be attributed to two aspects, the fitting distortion of Eq. (2) for the short-pulse situation induced by the slippage effects [39], and the potential deviations introduced by using slice-averaged parameters for power gain length calculations. Through numerical simulations, the slice beam properties can be optimized to simultaneously achieve localized small averaged beam size, energy spread, and high beam current, where the lasing occurs. Such optimization ensures more efficient electron-radiation interaction and facilitates energy extraction efficiency from the  $e$  beam.

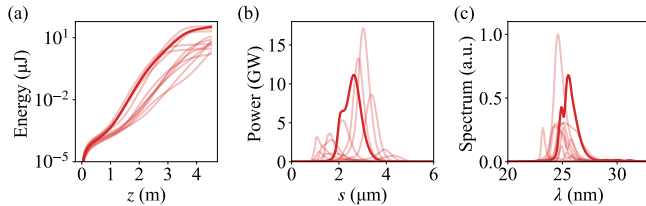


FIG. 4. Simulation results for FELs with the 13-electron-beam ensemble. (a) Radiation energy along the undulator. (b) Pulse duration and (c) spectrum of the generated radiation pulses at the exit of the undulator. The red solid line represents jitter-free, and the red transparent line represent different jitters. Each line represents the average value of 20 distinct simulations with random seeds.

Figure 4 presents the properties of the FEL radiation with the optimal operation targeting  $E_{min}$ . The evolution of the radiation along the undulator for the 13-electron-beam ensemble is shown in Fig. 4(a). A minority population enters the exponential gain regime near the 1-meter position of the undulator, while the majority initiates exponential growth beyond 1.5 meters, approaching saturation or approximate saturation at end of the undulator. Figure 4(b) illustrates the radiation power, indicating localized lasing due to the precisely designed beam-line parameters that impact localized phase-space characteristics through energy spread minimization and emittance matching, thereby enabling enhanced gain amplification dynamics. Notably, even the minimum radiation power maintains sub-GW level operation, demonstrating remarkable tolerance to system fluctuations. The corresponding radiation wavelength fluctuates with the RMS value of 0.8 nm, causing by the energy fluctuations of the accelerated  $e$ -beam, and thus the resonant wavelength, as

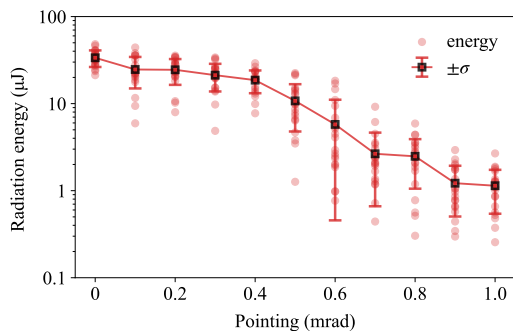


FIG. 5. Radiation energy as a function of beam pointing jitter. Mean values (black squares) and standard deviation (red error bars) derived from 20 independent simulations (red dots) with random seeds.

illustrated in Fig. 4(c). It should be noted that each line in Fig. 4 denotes the average value over 20 independent simulations with random seeds.

Beam pointing stability is another critical issue that must be addressed to ensure the robust operation of LWFA-driven FELs. To quantitatively evaluate the pointing instability, artificial angular kicks were introduced at the entrance of the beamline. Using  $e$  beams simulated under jitter-free conditions ( $\Delta_{RMS} = 0$ ), we artificially introduced angular deviations in both transverse planes ( $x' : 0.1 - 1.0$  mrad,  $y' : 0.1 - 1.0$  mrad). Figure 5 presents the quantitative analysis of radiation energy degradation caused by this angular perturbation range, revealing a monotonic decrease in output energy from 34  $\mu$ J in the jitter-free case to 1  $\mu$ J with a pointing deviation of 1 mrad. Even with a pointing deviation of 1 mrad, the average radiation energy, simulated over 20 random seeds, remains above 1  $\mu$ J. These results indicate that the proposed scheme exhibits remarkable tolerance to angular deviations.

In conclusion, we present a systematic design and optimization of compact LWFA-driven FELs with enhanced robustness and reliability. Through comprehensive start-to-end simulations, the feasibility of the proposed scheme has been demonstrated, achieving pulse energies exceeding 1  $\mu$ J under realistic experimental conditions. These simulations account for inherent parameter fluctuations, including laser energy variation, focal position displacement induced by wavefront distortion, and shock front position instability in the plasma. The optimized configuration exhibits remarkable tolerance to these critical parameter fluctuations while maintaining optimal phase space matching between the LWFA electron bunches and the undulator radiation field. These results establish crucial technical foundations for developing table-top FELs with unprecedented compactness, particularly highlighting robustness of the system against parameter jitter characteristic of current experimental configurations of LWFAs. To the best of our knowledge, the proposed

scheme represents the first demonstration of  $\mu$ J-level FEL radiation that is compatible with the stability issues of LWFA under actual experimental conditions.

This work was supported by National Natural Science Foundation of China (Grant Nos. 12388102, 12225411, 12474349, 12105353, 12174410 and 12434012), Strategic Priority Research Program of the Chinese Academy of Sciences (No. XDB0890201), CAS Project for Young Scientists in Basic Research (Grant No. YSBR060), Program of Shanghai Academic Research Leader (Grant No. 22XD1424200), the State Key Laboratory Program of the Chinese Ministry of Science and Technology and CAS Youth Innovation Promotion Association (2022242).

\* Contact author: fengke@siom.ac.cn

† Contact author: qwzhan@usst.edu.cn

‡ Contact author: wwt1980@siom.ac.cn

- [1] J. M. J. Madey, Stimulated emission of bremsstrahlung in a periodic magnetic field, *J. Appl. Phys.* **42**, 1906–1913 (1971).
- [2] P. Emma, R. Akre, J. Arthur, R. Bionta, C. Bostedt, J. Bozek, A. Brachmann, P. Bucksbaum, R. Coffee, F.-J. Decker, *et al.*, First lasing and operation of an ångström-wavelength free-electron laser, *Nat. Photonics* **4**, 641–647 (2010).
- [3] T. Ishikawa, H. Aoyagi, T. Asaka, Y. Asano, N. Azumi, T. Bizen, H. Ego, K. Fukami, T. Fukui, Y. Furukawa, *et al.*, A compact x-ray free-electron laser emitting in the sub-ångström region, *Nat. Photonics* **6**, 540–544 (2012).
- [4] H.-S. Kang, C.-K. Min, H. Heo, C. Kim, H. Yang, G. Kim, I. Nam, S. Y. Baek, H.-J. Choi, G. Mun, *et al.*, Hard x-ray free-electron laser with femtosecond-scale timing jitter, *Nat. Photonics* **11**, 708–713 (2017).
- [5] W. Decking, S. Abeghyan, P. Abramian, A. Abramsky, A. Aguirre, C. Albrecht, P. Alou, M. Altarelli, P. Altmann, K. Amyan, *et al.*, A mhz-repetition-rate hard x-ray free-electron laser driven by a superconducting linear accelerator, *Nat. Photonics* **14**, 391–397 (2020).
- [6] C. Bostedt, S. Boutet, D. M. Fritz, Z. Huang, H. J. Lee, H. T. Lemke, A. Robert, W. F. Schlotter, J. J. Turner, and G. J. Williams, Linac coherent light source: The first five years, *Rev. Mod. Phys.* **88**, 015007 (2016).
- [7] A. Burnett, M. Borghesi, A. Comley, M. Dean, S. Diaz-Moreno, D. Dye, J. Greenwood, A. Higginbotham, A. Kirrander, J. P. Marangos, *et al.*, *UK-XFEL Science Case*, Project Report (2020).
- [8] T. Tajima and J. M. Dawson, Laser electron accelerator, *Phys. Rev. Lett.* **43**, 267 (1979).
- [9] C. Bostedt, S. Boutet, D. M. Fritz, Z. Huang, H. J. Lee, H. T. Lemke, A. Robert, W. F. Schlotter, J. J. Turner, and G. J. Williams, Linac coherent light source: The first five years, *Rev. Mod. Phys.* **88**, 015007 (2016).
- [10] R. W. Assmann, M. K. Weikum, T. Akhter, D. Alesini, A. S. Alexandrova, M. P. Anania, N. E. Andreev, I. Andriyash, M. Artioli, A. Aschikhin, *et al.*, Eupraxia conceptual design report, *Eur. Phys. J. Spec. Top.* **229**, 3675–4284 (2020).
- [11] E. Esarey, C. B. Schroeder, and W. P. Leemans, Physics of laser-driven plasma-based electron accelerators, *Rev.*



- Mod. Phys. **81**, 1229 (2009).
- [12] A. J. Gonsalves, K. Nakamura, C. Lin, D. Panasenkov, S. Shiraishi, T. Sokollik, C. Benedetti, C. B. Schroeder, C. G. R. Geddes, J. van Tilborg, J. Osterhoff, E. Esarey, C. Toth, and W. P. Leemans, Tunable laser plasma accelerator based on longitudinal density tailoring, *Nat. Phys.* **7**, 862–866 (2011).
  - [13] S. Corde, C. Thauray, A. Lifschitz, G. Lambert, K. Ta Phuoc, X. Davoine, R. Lehe, D. Douillet, A. Rousse, and V. Malka, Observation of longitudinal and transverse self-injections in laser-plasma accelerators, *Nat. Commun.* **4**, 1501 (2013).
  - [14] A. Buck, J. Wenz, J. Xu, K. Khrennikov, K. Schmid, M. Heigoldt, J. M. Mikhailova, M. Geissler, B. Shen, F. Krausz, S. Karsch, and L. Veisz, Shock-front injector for high-quality laser-plasma acceleration, *Phys. Rev. Lett.* **110**, 185006 (2013).
  - [15] W. T. Wang, W. T. Li, J. S. Liu, Z. J. Zhang, R. Qi, C. H. Yu, J. Q. Liu, M. Fang, Z. Y. Qin, C. Wang, Y. Xu, F. X. Wu, Y. X. Leng, R. X. Li, and Z. Z. Xu, High-brightness high-energy electron beams from a laser wakefield accelerator via energy chirp control, *Phys. Rev. Lett.* **117**, 124801 (2016).
  - [16] M. C. Downer, R. Zgadzaj, A. Debus, U. Schramm, and M. C. Kaluza, Diagnostics for plasma-based electron accelerators, *Rev. Mod. Phys.* **90**, 035002 (2018).
  - [17] A. R. Maier, N. M. Delbos, T. Eichner, L. Hübner, S. Jalas, L. Jeppe, S. W. Jolly, M. Kirchen, V. Leroux, P. Messner, M. Schnepf, M. Trunk, P. A. Walker, C. Werle, and P. Winkler, Decoding sources of energy variability in a laser-plasma accelerator, *Phys. Rev. X* **10**, 031039 (2020).
  - [18] L. T. Ke, K. Feng, W. T. Wang, Z. Y. Qin, C. H. Yu, Y. Wu, Y. Chen, R. Qi, Z. J. Zhang, Y. Xu, X. J. Yang, Y. X. Leng, J. S. Liu, R. X. Li, and Z. Z. Xu, Near-gev electron beams at a few per-mille level from a laser wakefield accelerator via density-tailored plasma, *Phys. Rev. Lett.* **126**, 214801 (2021).
  - [19] A. Ferran Pousa, I. Agapov, S. A. Antipov, R. W. Assmann, R. Brinkmann, S. Jalas, M. Kirchen, W. P. Leemans, A. R. Maier, A. Martinez de la Ossa, J. Osterhoff, and M. Thévenet, Energy compression and stabilization of laser-plasma accelerators, *Phys. Rev. Lett.* **129**, 094801 (2022).
  - [20] J. Götzfried, A. Döpp, M. F. Gilljohann, F. M. Foerster, H. Ding, S. Schindler, G. Schilling, A. Buck, L. Veisz, and S. Karsch, Physics of high-charge electron beams in laser-plasma wakefields, *Phys. Rev. X* **10**, 041015 (2020).
  - [21] W. Wang, K. Feng, L. Ke, C. Yu, Y. Xu, R. Qi, Y. Chen, Z. Qin, Z. Zhang, M. Fang, J. Liu, K. Jiang, H. Wang, C. Wang, X. Yang, F. Wu, Y. Leng, J. Liu, R. Li, and Z. Xu, Free-electron lasing at 27 nanometres based on a laser wakefield accelerator, *Nature* **595**, 516–520 (2021).
  - [22] M. Labat, J. C. Cabadağ, A. Ghaith, A. Irman, A. Berlioux, P. Berteaud, F. Blache, S. Bock, F. Bouvet, F. Briquez, *et al.*, Seeded free-electron laser driven by a compact laser plasma accelerator, *Nat. Photonics* **17**, 150–156 (2022).
  - [23] Z. Huang and K.-J. Kim, Review of x-ray free-electron laser theory, *Phys. Rev. ST Accel. Beams* **10**, 034801 (2007).
  - [24] M. Galletti, R. Assmann, M. E. Couprie, M. Ferrario, L. Giannessi, A. Irman, R. Pompili, and W. Wang, Prospects for free-electron lasers powered by plasma-wakefield-accelerated beams, *Nat. Photonics* **18**, 780–791 (2024).
  - [25] J. Duris, D. Kennedy, A. Hanuka, J. Shtalenkova, A. Edehlen, P. Baxevanis, A. Egger, T. Cope, M. McIntire, S. Ermon, and D. Ratner, Bayesian optimization of a free-electron laser, *Phys. Rev. Lett.* **124**, 124801 (2020).
  - [26] S. Jalas, M. Kirchen, P. Messner, P. Winkler, L. Hübner, J. Dirkwinkel, M. Schnepf, R. Lehe, and A. R. Maier, Bayesian optimization of a laser-plasma accelerator, *Phys. Rev. Lett.* **126**, 104801 (2021).
  - [27] M. Kirchen, S. Jalas, P. Messner, P. Winkler, T. Eichner, L. Hübner, T. Hülsenbusch, L. Jeppe, T. Parikh, M. Schnepf, and A. R. Maier, Optimal beam loading in a laser-plasma accelerator, *Phys. Rev. Lett.* **126**, 174801 (2021).
  - [28] E. J. Dolier, M. King, R. Wilson, R. J. Gray, and P. McKenna, Multi-parameter bayesian optimisation of laser-driven ion acceleration in particle-in-cell simulations, *New J. Phys.* **24**, 073025 (2022).
  - [29] F. Irshad, S. Karsch, and A. Döpp, Multi-objective and multi-fidelity bayesian optimization of laser-plasma acceleration, *Phys. Rev. Res.* **5**, 013063 (2023).
  - [30] A. Döpp, C. Eberle, S. Howard, F. Irshad, J. Lin, and M. Streeter, Data-driven science and machine learning methods in laser-plasma physics, *High Power Laser Sci. Eng.* **11**, e55 (2023).
  - [31] R. Lehe, M. Kirchen, I. A. Andriyash, B. B. Godfrey, and J.-L. Vay, A spectral, quasi-cylindrical and dispersion-free particle-in-cell algorithm, *Computer Physics Communications* **203**, 66 (2016).
  - [32] S. Jalas, I. Dornmair, R. Lehe, H. Vincenti, J.-L. Vay, M. Kirchen, and A. R. Maier, Accurate modeling of plasma acceleration with arbitrary order pseudospectral particle-in-cell methods, *Phys. Plasmas* **24**, 033115 (2017).
  - [33] K. Feng, K. Jiang, R. Hu, C. Lv, X. Chen, H. Jiang, S. Luan, W. Wang, and R. Li, High-quality electron beam generation from laser wakefield accelerators for driving compact free electron lasers, *arXiv:2501.09916*.
  - [34] F. Wu, Z. Zhang, X. Yang, J. Hu, P. Ji, J. Gui, C. Wang, J. Chen, Y. Peng, X. Liu, Y. Liu, X. Lu, Y. Xu, Y. Leng, R. Li, and Z. Xu, Performance improvement of a 200TW/1Hz ti:sapphire laser for laser wakefield electron accelerator, *Opt. Laser Technol.* **131**, 106453 (2020).
  - [35] N. Hansen, The cma evolution strategy: A tutorial, *arXiv:1604.00772*.
  - [36] T. Akiba, S. Sano, T. Yanase, T. Ohta, and M. Koyama, Optuna: A next-generation hyperparameter optimization framework, in *Proceedings of the 25th ACM SIGKDD International Conference on Knowledge Discovery & Data Mining, KDD '19* (ACM, New York, NY, USA, 2019) p. 2623–2631.
  - [37] M. Borland, *ELEGANT: A flexible SDDS-compliant code for accelerator simulation*, Tech. Rep. (Argonne National Lab., IL (US), 2000).
  - [38] S. Reiche, Genesis 1.3: a fully 3d time-dependent fel simulation code, *Nucl. Instrum. Methods Phys. Res. A* **429**, 243 (1999).
  - [39] C. Pellegrini, A. Marinelli, and S. Reiche, The physics of x-ray free-electron lasers, *Rev. Mod. Phys.* **88**, 015006 (2016).

## Appendix A: Measurement of shock front

The shock front is essential for the injection process in LWFA and thus significantly impacts the beam quality. As previously discussed, the position jitter with an RMS value of 4.9  $\mu\text{m}$  was used in our simulations, which was experimentally measured. To capture the shock front properties, a probe laser passed through the plasma region and imaged using a 4f imaging system before entering the interferometer. The resulting interference patterns were captured using a charged-coupled device (CCD), with the shock front region depicted in Fig. 6(a). The corresponding phase distribution and the first-order derivative of the fringe phase are illustrated in Figs. 6(b) and 6(c), respectively. To characterize the position jitter of the shock front, we performed continuous acquisition of 100 experimental shots, as shown in Fig. 6(d). An RMS value of  $\sigma_{z\text{shock}} = 4.9 \mu\text{m}$  was obtained. The statistical parameter is represented in the red shaded region in Fig. 6(d), providing quantitative analysis of the shock wave stability.

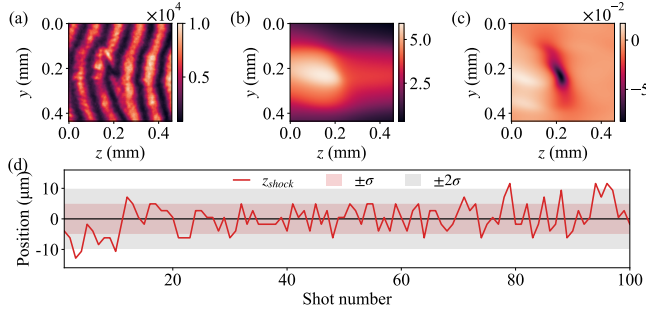


FIG. 6. Properties of the measured shock front. (a) Measured interferometric fringe patterns and (b)-(c) the corresponding distributions of phase (b) and its first-order derivative (c). (d) Statics on the shock front jitter over consecutive 100 shots based on the first derivative of phase. The red and gray shaded region denotes the RMS and  $\pm 2$  times RMS range, respectively.

## Appendix B: Gain length optimization

The 3D power gain length  $L_G$  is a fundamental figure of merit for characterizing FEL performance, defined by  $L_G = L_{G0}(1 + \Lambda)$ , where  $L_{G0} = \lambda_u/(4\sqrt{3}\pi\rho)$  is the 1D power gain length,  $\lambda_u$  is the period length of the undulator,  $\rho$  is the dimensionless Pierce parameter defined by:

$$\rho = \frac{1}{\gamma_0} \left( \frac{1}{16} \frac{I_p}{I_A} \frac{K_0^2 [JJ]^2}{K_u^2 \sigma_x \sigma_y} \right)^{\frac{1}{3}}. \quad (1)$$

and  $\Lambda$  is the degradation factor of gain length given by the fitting formula [23]:

$$\Lambda = 0.45\eta_d^{0.57} + 0.55\eta_\epsilon^{1.6} + 3\eta_\gamma^2 + 0.35\eta_\epsilon^{2.9}\eta_\gamma^{2.4} \quad (2)$$

$$+ 51\eta_d^{0.95}\eta_\gamma^3 + 5.4\eta_d^{0.7}\eta_\epsilon^{1.9} + 1140\eta_d^{2.2}\eta_\epsilon^{2.9}\eta_\gamma^{3.2}$$

where  $\eta_d$ ,  $\eta_\epsilon$  and  $\eta_\gamma$  are three scaled parameters quantifies the diffraction, angular spread and energy spread effects, respectively, and can be written as:

$$\eta_d = \frac{L_{G0}}{2k_r \sigma_x \sigma_y}, \quad (3)$$

$$\eta_\epsilon = \frac{L_{G0}}{2k_r \sqrt{\beta_x \beta_y} \sqrt{\epsilon_x \epsilon_y}}, \quad (4)$$

$$\eta_\gamma = \frac{L_{G0}}{4\pi \lambda_u \sigma_\eta}. \quad (5)$$

where  $\gamma_0$  is the electron energy in units of the rest energy,  $I_p$  is the peak current,  $I_A = 17 \text{ kA}$  is the Alfvén current,  $K_0$  is the undulator parameter,  $[JJ] = [J_0(\xi) - J_1(\xi)]$  with  $\xi = K_0^2/(4 + 2K_0^2)$  is the Bessel function factor for a planar undulator,  $K_u = 2\pi/\lambda_u$ ,  $k_r = 2\pi/\lambda_r$ ,  $\lambda_r = \lambda_u(1 + K_0^2/2)/(2\gamma_0^2)$  is radiation wavelength,  $\sigma_x$  and  $\sigma_y$  is the average beam size in the undulator,  $\beta_x$  and  $\beta_y$  is the average Twiss parameter in the undulator,  $\epsilon_x$  and  $\epsilon_y$  is the average emittance in the undulator, and  $\sigma_\eta$  is the relative RMS slice energy spread. The parameters  $\gamma_0$ ,  $I_p$ , and  $\sigma_\eta$  were obtained from FBPIC numerical simulations, whereas the transverse beam characteristics  $\sigma_x$ ,  $\sigma_y$ ,  $\beta_x$ ,  $\beta_y$ ,  $\epsilon_x$ , and  $\epsilon_y$  were derived from particle tracking simulations using the ELEGANT code [37].

In the optimization framework targeting  $\langle L_G^{-1} \rangle$ , we conducted parallel particle tracking simulations utilizing the 13-electron-beam ensemble illustrated in Fig. 1. The resulting transverse beam characteristics were subsequently employed to calculate  $\langle L_G^{-1} \rangle$ , which serves as the primary quantitative metric for objective function evaluation. The parameter ranges for the optimization are presented in Table II.

TABLE II. Parameter space used in  $\langle L_G^{-1} \rangle$  optimization.

Parameter	Min. value	Max. value	Best value <sup>a</sup>
$l_0$	0.03	1.0	0.08
$l_1$	0.03	1.0	0.11
$l_2$	0.03	1.0	0.16
$l_3$	0.3	3.0	1.17
$l_4$	0.3	3.0	2.98
$l_5$	0.3	3.0	0.39
$l_6$	0.3	3.0	0.33
$q_1$	-143	143	-139
$q_2$	-143	143	141
$q_3$	-143	143	-69
$q_4$	-45	45	-0.34
$q_5$	-45	45	10.51
$q_6$	-45	45	-10.82

<sup>a</sup> Note  $l_0 - l_6$  in units of meters (m),  $q_1 - q_6$  in units of per square meter ( $\text{m}^{-2}$ ).

Figure 7(a) illustrates the evolution of the objective function  $\langle L_G^{-1} \rangle$  throughout the BO process, with

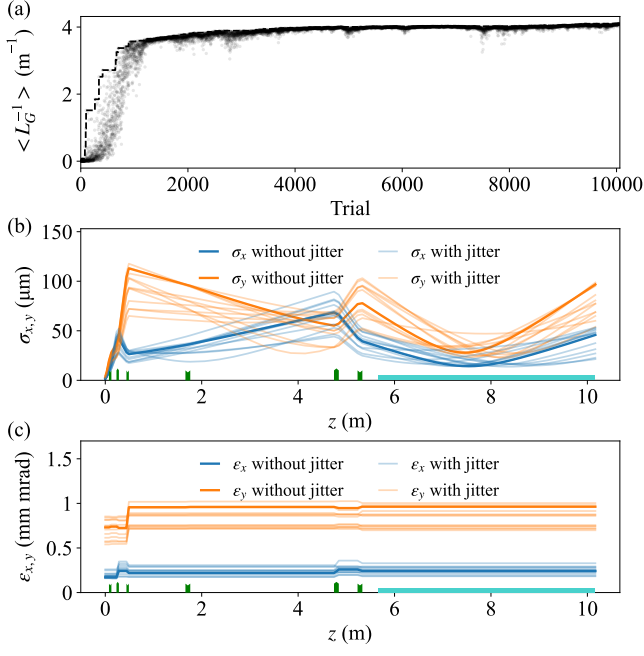


FIG. 7. The optimization results of the  $\langle L_G^{-1} \rangle$ . (a) The simulated objective function  $\langle L_G^{-1} \rangle$  (dots) with the cumulative best results (black dashed line). (b)-(c) The evolution of the beam size (b) and the normalized projected emittance (c) along the beamline in horizontal (blue) and vertical (orange) directions. The tracking beamline was configured using the best parameters obtained from the optimization.

the cumulative optimal results represented by the black dashed line. The optimization commenced with random sampling within the predefined parameter space detailed in Table II. A progressive convergence of the objective function emerges after approximately 1200 iterations, with the optimal solution achieved at iteration 10,071, corresponding to an average 3D power gain length of approximately 0.24 m. The resulting beam sizes and transverse emittance for the 13-electron-beam ensemble under the optimized conditions are presented in Figs. 7(b) and 7(c), respectively. It should be noted that slice-averaged energy spread of the  $e$  beam is employed when calculating the power gain length. The radiation gain predominantly originates from specific slices with advanced beam qualities, while other slices contribute minimally to the overall gain. The optimization based on slice-averaged values may cause potential deviations, considering the different properties over slices of the  $e$  beam from LW-FAs. To address this limitation, the optimization using the radiation energy as an alternative objective function is implemented.